

The Circumstellar Envelope of the Semiregular Variable Star V CVn

B. S. Safonov^{1*}, A. V. Dodin¹, S. A. Lamzin¹, and A. S. Rastorguev^{2,1}

¹*Sternberg Astronomical Institute, Moscow State University, Universitetskii pr. 13, Moscow, 119992 Russia*

²*Faculty of Physics, Moscow State University, Moscow, 119992 Russia*

Received April 22, 2019; revised May 6, 2019; accepted May 28, 2019

Abstract—V CVn is a red semiregular variable star with an amplitude of its *V*-band brightness variations of $\approx 2^m$. An unusually high amplitude of its polarization variability, up to 6%, a noticeable inverse correlation between polarization and total flux, and relative constancy of the angle of polarization distinguish this star from other semiregular variables. To clarify the nature of these peculiarities, we have observed the object with the 2.5-m telescope at the Caucasian Observatory of the Sternberg Astronomical Institute of the Moscow State University using differential speckle polarimetry at wavelengths of 550, 625, and 880 nm. The observations were performed on 20 dates distributed over three pulsation periods. We have detected an asymmetric reflection nebula around the star at a distance of ≈ 35 mas. Three regions that change their brightness with the same characteristic time scale as the star, but with different phase shifts are identified in the nebula. We consider several hypotheses that could explain this behavior.

DOI: 10.1134/S1063773719070065

Keywords: *circumstellar envelopes, stars: pulsations, methods: high angular resolution.*

INTRODUCTION

The radiation from red long-period variable stars is often polarized due to its scattering by the dust forming in their cool atmospheres. The degree and angle of polarization exhibit an irregular variability attributable to continuous chaotic changes in the envelopes of these stars. The polarization fraction usually varies from 0 to 2%, while the time scales of these changes range from a month to several years (Clarke 2010). The semiregular variable star V CVn with a period of 194^d and an amplitude of its *V*-band brightness variations of $\approx 2^m$ (Samus' et al. 2017) stands out against this background. The degree of polarization of its radiation can reach 6%, but the angle of polarization is quite stable and changes from 99° to 122° (Serkowski and Shawl 2001). In addition, V CVn exhibits the most prominent inverse correlation between flux and polarization fraction among all long-period variable stars.

Neilson et al. (2014) studied in detail the pattern of polarization variability in V CVn and qualitatively considered several hypotheses that could explain the unique behavior of the star. They concluded that the dusty disk and bow shock models are the most plausible ones. In the first case, the intrinsic polarization is generated due to the scattering by a thick dusty disk or torus. The observer is close to

the equatorial plane of this structure. The second hypothesis suggests that the stellar wind from V CVn produces a bow shock similar to the one observed around *o* Cet when interacting with the interstellar medium (Martin et al. 2007). Dust in the wind will be accumulated in the bow shock region, scatter, and polarize the observed radiation from the object.

In both cases, the shape of the resulting dust envelope deviates considerably from the centrally symmetric one, which can give a significant total polarization whose orientation will be very stable. Neilson et al. (2014) showed how the interaction between the pulsation-driven density waves and a dusty disk or dusty bow shock could qualitatively explain the observed inverse correlation between flux and polarization.

So far only the integrated polarization properties of V CVn have been investigated and a large number of measurements have been made at various pulsation phases of the star. In this case, however, the polarization was averaged over an object that could have a complex structure, which makes it difficult to interpret its behavior. In such cases, the spatial localization of the polarized radiation can be the key to understanding the object.

In this paper we present our measurements of the spatial distribution of polarization radiation from V CVn obtained with a high angular resolution at several epochs. We resolved with confidence the

*E-mail: safonov@sai.msu.ru

Table 1. Observations of V CVn and the results of their approximation by the model of three arcs (Fig. 2)

JD ^a	Band	mag ^b	p , % ^c	θ , deg ^c	Polarized flux, 10^{-2} ^d			χ_r^2
					NNE	SSE	SSW	
2458090.6	550	7.1	0.90 ± 0.15	106 ± 10	$0.22^{+0.03}_{-0.01}$	$0.35^{+0.02}_{-0.02}$	$0.66^{+0.02}_{-0.02}$	1.7
2458090.6	625	5.9	0.93 ± 0.15	107 ± 9	$0.26^{+0.03}_{-0.01}$	$0.28^{+0.03}_{-0.01}$	$0.62^{+0.02}_{-0.01}$	2.0
2458090.6	880	3.7	0.70 ± 0.15	104 ± 12	$0.27^{+0.10}_{-0.01}$	$0.14^{+0.05}_{-0.01}$	$0.38^{+0.04}_{-0.01}$	3.0

A complete version of the table is accessible in electronic form.

^a JD is given for the series center.

^b The magnitude is given in the observation band. It was estimated from quasi-simultaneous observations of the nonvariable star HIP65550, for which we adopted the following magnitudes in the 550, 625, and 880 nm bands: 5.9, 5.1, and 4.9, corresponding to its V , R , and I magnitudes.

^c The degree and angle of polarization were estimated from the series used for the reduction by differential speckle polarimetry.

^d The polarized fluxes from the envelope component arcs relative to the total flux from the object; the 1σ uncertainty is given.

circumstellar envelope responsible for the high and variable polarization of the star. The behavior of this envelope explains the unusual polarization properties of V CVn.

First we describe the method and our observations and then present a simple geometric model within the framework of which we determine the envelope parameters. Thereafter, we discuss possible physical interpretations of the observations. The results of our studies are summarized in the Conclusions.

OBSERVATIONS

We observed V CVn with the SPeckle Polarimeter (SPP) of the 2.5-m telescope at the Caucasian Observatory of the Sternberg Astronomical Institute. The SPP is a combination of a two-beam polarimeter and a visible-range speckle interferometer (Safonov et al. 2017). The instrument is designed to study the distribution of polarized radiation from astrophysical objects at a diffraction-limited resolution, i.e., ≈ 50 mas at a wavelength of 500 nm. The angular scale of the SPP camera is 20.6 mas/pix.

The observations were performed on 20 dates distributed over three stellar pulsation periods between March 2017 and January 2019 (see Table 1). The regime of fast polarimetry was applied; three medium-band filters centered at 550, 625, and 880 nm were used. The observations in March and May 2017 were carried out in the V and I_c filters.

The observations were reduced by the method of differential speckle polarimetry described by Safonov et al. (2019). This method gives estimates for the

ratios of the object's visibilities in two orthogonal polarizations (Norris et al. 2012):

$$\begin{aligned}\mathcal{R}_Q(\mathbf{f}) &= \frac{\tilde{I}(\mathbf{f}) + \tilde{Q}(\mathbf{f})}{\tilde{I}(\mathbf{f}) - \tilde{Q}(\mathbf{f})}, \\ \mathcal{R}_U(\mathbf{f}) &= \frac{\tilde{I}(\mathbf{f}) + \tilde{U}(\mathbf{f})}{\tilde{I}(\mathbf{f}) - \tilde{U}(\mathbf{f})},\end{aligned}\quad (1)$$

where \tilde{I} , \tilde{Q} , and \tilde{U} are the Fourier transforms of the distributions of Stokes parameters in the object, and \mathbf{f} is the spatial frequency vector. One can see that two ratios can be determined: \mathcal{R}_Q and \mathcal{R}_U for the Stokes parameters Q and U , respectively. Differential speckle polarimetry allows both the amplitude and the phase of \mathcal{R} to be estimated. The observations were performed at the Cassegrain and Nasmyth foci of the telescope. In the latter case, the measurements were corrected for the instrumental polarization effects (Safonov et al. 2019).

The \mathcal{R} measurements in two filters made on two dates are presented in Fig. 1. \mathcal{R} is seen to deviate significantly from unity and, consequently, the polarized flux is resolved.

Safonov et al. (2019) showed how the distributions of the corresponding Stokes parameters in an object could be estimated from the \mathcal{R} measurements. In turn, the polarized intensity and the angle of polarization can be estimated from the Stokes parameters. These values are presented in Fig. 1 in the lower row.

It can be seen from Fig. 1 that the so-called azimuthal polarization pattern dominates in the envelope. The plane of polarization of some envelope

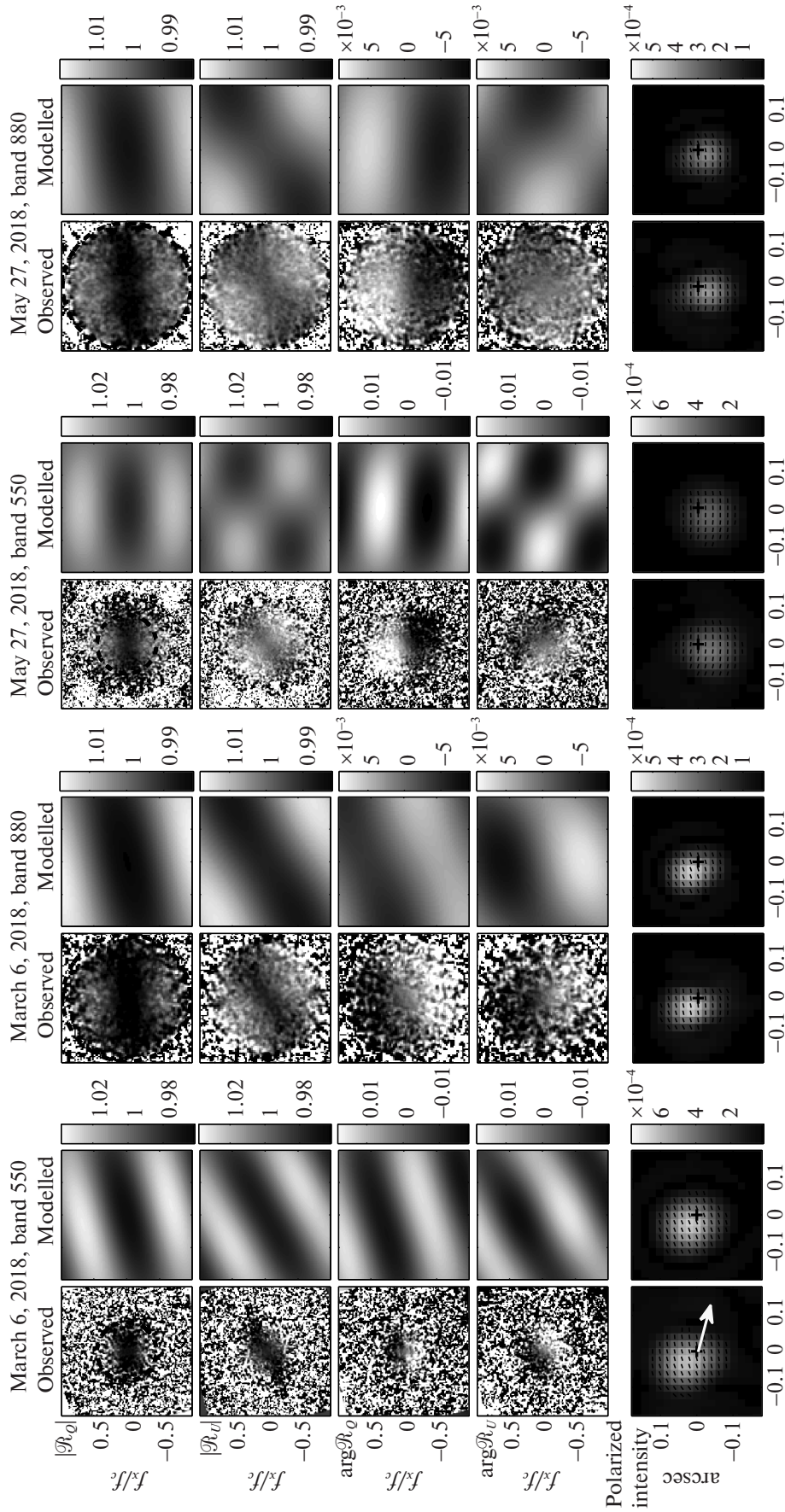


Fig. 1. The results of our observations of V CVn by differential speckle polarimetry and their modeling (see the corresponding subsection) are presented in the odd and even columns, respectively. The columns are: 1–2 for the 550-nm band on March 6, 2018; 3–4 for the 880-nm band on March 6, 2018; 5–6 for the 550-nm band on May 27, 2018; 7–8 for the 880-nm band on May 27, 2018. The four upper rows are: $|R_Q|$, $|R_U|$, $\arg R_Q$, and $\arg R_U$ (see Eq. (1)). The spatial frequencies normalized to the cutoff frequency of the optical system D/λ , where D is the aperture diameter and λ is the wavelength, are plotted along the axes for them. The dashed circle in the upper row denote the frequency domain where the observations and the model were compared. The distributions of the polarized intensity per pixel (the angular size of a pixel is 20.6 mas) with respect to the total flux from the object are presented in the lower row. The short lines indicate the polarization orientation; their length is arbitrary. In the lower row the angular coordinates are along the axes. The white arrow indicates the direction of the star's proper motion. Everywhere the north is up and the east is to the left. The same images for all filters and all dates can be found at http://infml.sai.msu.ru/kgg/mfc_VCVn_en.php.

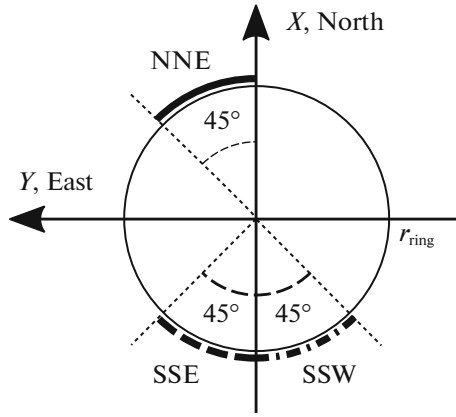


Fig. 2. The model for the circumstellar envelope of V CVn that was used to approximate the observations: three scattering arcs with a vertex angle of 45° at fixed position angles. The elementary segments of the arcs are polarized perpendicularly to the direction toward the star.

surface element is perpendicular to the direction connecting this surface element and the star. Consequently, the envelope is most likely a reflection nebula, i.e., it scatters the stellar radiation. The observations performed on the same night, but in different filters show good agreement. On the other hand, the difference in the observations performed on different dates is drastic. For example, on March 5, 2018, the nebula was dominated by the region to the north-northeast (NNE) of the star. Only 82 days later, on May 27, 2018, the region to the south-southeast (SSE) became brighter than the northern one. On some other dates the region to the south-southwest (SSW) became brightest (the images for all filters and all dates of observations are provided at http://lnfm1.sai.msu.ru/kgomfc_VCVn_en.php).

The nebula detected by us has a characteristic angular size comparable to the diffraction-limited resolution of the telescope. Therefore, the images presented in the lower row of Fig. 1 are strongly blurred by the point spread function of the optical system. Because of this and some other image reconstruction problems, these images can be interpreted only qualitatively. A quantitative interpretation of the observations will be made in terms of \mathcal{R} in the next section.

MODELING

Based on the images of the object in polarized light, we assumed that it could be described by a model consisting of an unpolarized central star and three scattering arcs (Fig. 2). The configuration of these arcs is fixed. We will denote them in accordance with their positions relative to the star: NNE, SSE, and SSW. The elementary segments of the arcs are polarized perpendicularly to the direction toward the star.

Within the framework of this model the object's observation in one filter and on one date is described by four parameters: the radius of the arcs r_e and the ratios of their polarized fluxes to the total flux from the object: F_{NNE} , F_{SSE} , and F_{SSW} . The polarized flux is the product of the degree of polarization and the normal flux. These parameters specify the distribution of the Stokes parameters I , Q , and U in the object, from which the expected \mathcal{R}_Q and \mathcal{R}_U can be calculated using Eqs. (1). Note that within the framework of the method used by us it is impossible to independently estimate the polarization fraction of the arcs and the fluxes from them—only the product of these quantities, i.e., the polarized flux, is measurable.

We compared the model and observed values of \mathcal{R} by calculating the residual with a weight $1/\sigma^2$, where σ is the uncertainty in the \mathcal{R} estimate (an example is given in Safonov et al. (2019)). The residual was summed in the frequency domain where the signal-to-noise ratio for \mathcal{R} is sufficiently high (Fig. 1). We searched for an optimal model by minimizing the total residual.

We assumed the radius of the arcs r_e to be independent of time and wavelength and determined it by the joint approximation of the observations in three filters carried out on two dates: March 6, 2018 and May 27, 2018. It was found to be 35 ± 1 mas. Since r_e is less than the formal diffraction-limited resolution of the telescope, we cannot perform a model-independent reconstruction of the envelope image. The quantity r_e is conditional; it would be different, for example, in the model of sectors rather than arcs. Nevertheless, the deviation of the polarized sources from a point-like star and their extent are detected quite reliably, and r_e may be considered as a characteristic size of the envelope.

Having fixed $r_e = 35$ mas, we approximated each observation individually by varying the remaining three parameters F_{NNE} , F_{SSE} , and F_{SSW} . Examples of the model values of \mathcal{R} and the corresponding images are given in Fig. 1 in the even columns. The results of our approximation of all observations are presented in Table 1. For 39 of the 57 observations the χ^2 value is less than 3 and, consequently, the model describes the observations with a reasonable accuracy. This can also be made sure by looking at Fig. 1.

The total polarized flux from the envelope accounts for 0.01–0.03 of the total flux from the object. In other words, the envelope explains the object's polarization, but, at the same time, the unpolarized stellar radiation dominates the total flux.

The behavior of the envelope components in the 550-nm band is illustrated in Fig. 3. For the convenience of comparison, the AAVSO light curve of

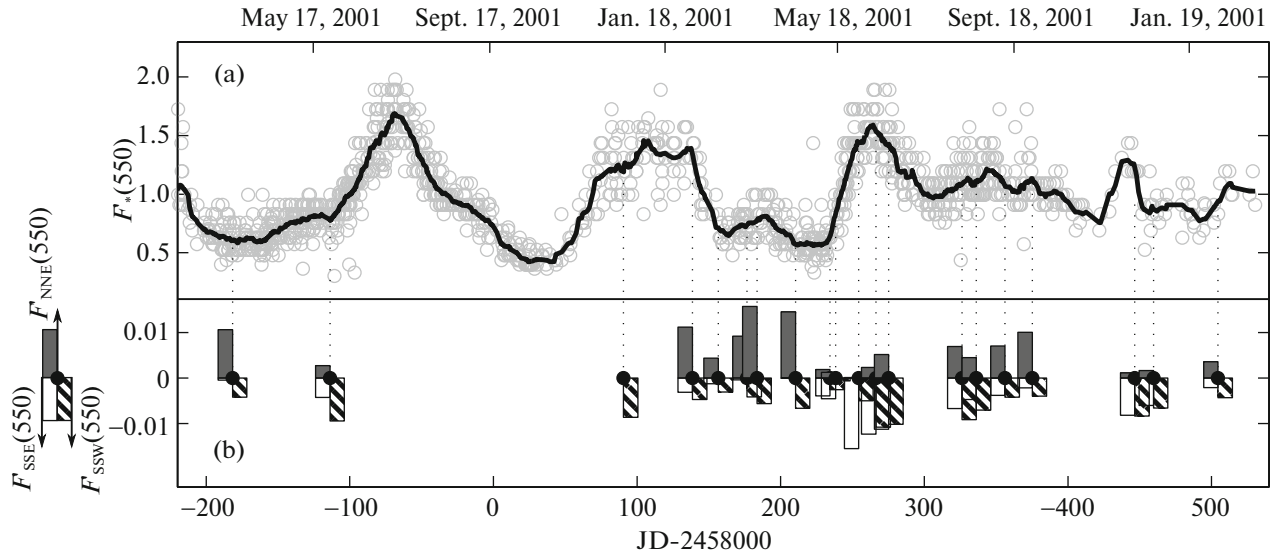


Fig. 3. (a) Individual visual magnitude estimates from the AAVSO database converted to the flux and normalized to the average level (gray circles). The thick black line indicates a moving average of the AAVSO fluxes. (b) The columns denote the polarized flux from the envelope components. The columns painted in gray, white, and diagonal lines correspond to the NNE, SSE, and SSW arcs, respectively. The column height corresponds to the polarized flux from them normalized to the average (unpolarized) flux from the star. The height is measured from the zero level upward for the NNE arc and downward for the SSE and SSW arcs.

V CVn (Kafka 2018) is given on the same graph. Note that the polarized fluxes from the arcs in this figure are normalized to the object's average flux and not to its current value. This allows the variability of the arcs to be considered independently of the star's variability.

It follows from Fig. 3 that when the star is at minimum brightness, the NNE arc is brightest, while the NNE arc dims as the star brightens. This leads to a rise in the total polarization of the object at minimum brightness. At the same time, the SSE and SSW arcs change their brightness synchronously with the star.

To a first approximation, these features are repeated in all of the three observed pulsation cycles. However, the exact repetition is not expected anyway, because the stellar pulsations are not quite regular. For example, in the period between $JD = 2458260$ and $JD = 2458440$ there was virtually no prominent brightness minimum. The polarization fraction remained less than 2%. The difference in arc brightnesses in this period was less distinct than in the previous period, but the overall pattern of arc brightness variations remained as before.

DISCUSSION

The distance to V CVn is 1.27 ± 0.24 kpc (Gaia 2018), with the star lying quite high above the Galactic plane: 1.17 ± 0.23 kpc. The apparent proper motion of V CVn is $\mu_\alpha \cos \delta = -38.99 \pm 0.20$ mas yr $^{-1}$ and $\mu_\delta = -11.77 \pm 0.21$ mas yr $^{-1}$, corresponding to

a tangential velocity of 251 km s^{-1} relative to the Sun. The radial velocity of the star is 4.7 km s^{-1} (Famaey et al. 2009), i.e., the star moves almost perpendicularly to the line of sight.

The star has a parallax error of 0.14 mas, which is triple the median of this quantity for $G \approx 8.5$ stars (Lindgren et al. 2018). The proper motion error is also large. The additional noise of astrometry can be caused both by the chromatic instrumental effects inherent in the Gaia data and by the behavior of the star's envelope described in the previous section.

According to Sharma et al. (2016), the spectral type of V CVn is M6 III and its effective temperature is 3180 ± 99 K. The luminosity corresponding to the Gaia distance is $3.6 \pm 1.5 \times 10^4 L_\odot$ (McDonald et al. 2012). The radius of the star calculated from these data is $R_\star = 590 \pm 110 R_\odot$, corresponding to an angular radius of 2.2 mas at the object's distance.

The characteristic linear size of the nebula found is 44 ± 10 AU, which is greater than R_\star approximately by a factor of 10. Thus, the observed polarized flux is formed in the circumstellar envelope at a considerable distance from the photosphere. It is reasonable to assume that this envelope is produced by a dusty stellar wind. The mid-infrared excess (Price et al. 2010) and the silicate feature at $9.7 \mu\text{m}$ (Olson et al. 1986; Simpson 1991) also provide evidence for the presence of a dusty envelope. At the same time, the star has quite a small color excess, $E(B - V) = 0.04$ (Montez et al. 2017), and, consequently, this envelope cannot be spherically symmetric.

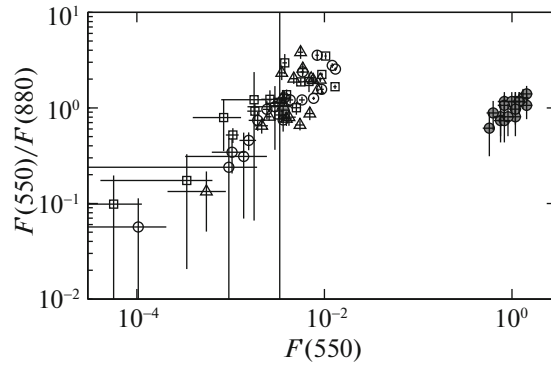


Fig. 4. Color–flux diagrams for the envelope components and the entire object. The flux in the 550-nm filter normalized to the average total flux in this filter is plotted along the horizontal axis. The ratio of the normalized fluxes in the 550- and 880-nm filters is plotted along the OY axis. The open circles, squares, and triangles correspond to the NNE, SSE, and SSW arcs, respectively. The filled circles correspond to the object as a whole, but, actually, characterize the behavior of the star, because it makes a major contribution to the unpolarized flux. The polarized fluxes are given for the envelope components; the total fluxes are given for the entire object.

The orbital motion could be the simplest explanation for the brightness variations of different parts of the envelope. However, passing a semicircle with a radius of 44 AU in half the stellar pulsation period, $P \approx 194^d$ (Samus’ et al. 2017), requires a velocity of $\approx 2500 \text{ km s}^{-1}$. This value is much greater than the corresponding Keplerian velocity (at a stellar mass $M < 10 M_{\odot}$). Therefore, this explanation is unsuitable and we will consider other interpretations of the observed properties of the envelope found by us.

Bow Shock Hypothesis

Neilson et al. (2014) supposed that an asymmetric dust envelope could emerge behind the bow shock formed at the boundary between the stellar wind and the incoming flow of the interstellar medium. The distance between the star and the apex of this bow shock is determined by the equality between the ram pressures of the stellar wind and the gas flow (van Buren and McCray 1988). Let us estimate the interstellar medium density at which the bow shock will be located at a distance of ~ 40 AU from the star.

For this purpose, we will need the mass loss rate in the stellar wind. This quantity can be estimated from the pulsation period P using the relation proposed by De Beck et al. (2010). For V CVn the expected mass loss rate is $\sim 2 \times 10^{-7} M_{\odot} \text{ yr}^{-1}$.

To estimate the velocity of the star relative to the interstellar medium, V_* , we made a correction for the Galactic differential rotation and the solar motion toward the apex using the maser rotation curve, which is closest to the gas kinematics (Rastorguev et al. 2017). It turned out that the velocity of the star relative to the local standard of rest is $V_* \approx 237 \text{ km s}^{-1}$, while the position angle of its projection

onto the plane of the sky is 255° —this direction is indicated by the arrow on the lower left panel of Fig. 1.

Substituting V_* into Eq. (1) from van Buren and McCray (1988), we obtain the following expression relating the required interstellar medium density and the stellar wind velocity V_w :

$$n_H = 490V_w, \quad (2)$$

where V_w is in km s^{-1} and the density is in cm^{-3} . At a stellar wind velocity of a few km s^{-1} , typical for this type of stars, the density n_H should be $\sim 10^3 \text{ cm}^{-3}$.

However, n_H at 1.2 kpc above the Galactic plane is $\sim 3 \times 10^{-3} \text{ cm}^{-3}$, the “best estimate” from Fig. 10 in Dickey and Lockman (1990). In accordance with the HI map from Ben Bekhti et al. (2016), there are no molecular clouds toward V CVn. We conclude that the interstellar gas density in the vicinity of V CVn is approximately five orders of magnitude lower than is required for the bow shock formation at a distance of ~ 40 AU from the star. In other words, the bow shock must emerge at distances much greater than the size of the envelope detected by us. However, an initially spherically symmetric stellar wind should retain this symmetry up to the region where the bow shock emerges. Therefore, in our case, the interaction of the stellar wind with the surrounding medium should not lead to an asymmetry of the dust envelope and, a fortiori, a variability of its surface brightness. The anisotropy of the stellar mass loss is more likely responsible for the envelope shape.

Light Echo Hypothesis

The fact that the brightness of the NNE arc reaches its maximum $\Delta t \sim 95^d$ after the star’s brightness maximum can be explained by the light echo effect, as, for example, in RS Pup (Kervella et al. 2008).

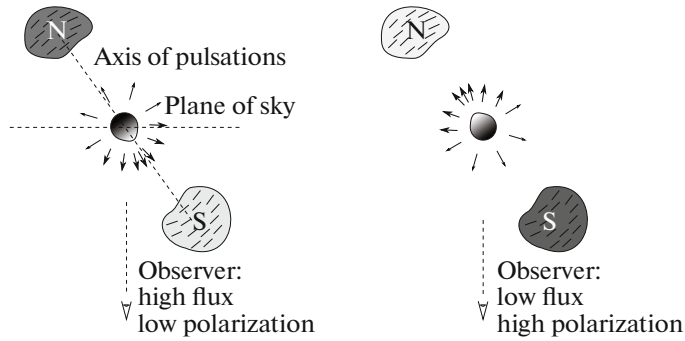


Fig. 5. Scheme of the object in the nonradial pulsation model (not to scale) at the maximum (left) and minimum (right) brightness of the star from the point of view of an Earth-based observer.

In this case, the NNE arc should be at least $c\Delta t/2 \sim 8000$ AU farther from us than the star. The characteristic linear size of the corresponding cloud can be estimated as the NNE arc length: ≈ 40 AU. This circumstellar cloud intercepts no more than $\approx 1.4 \times 10^{-6}$ of the stellar radiation. Some fraction of this radiation will be absorbed, while the remaining one will be scattered mostly forward. For the observer the cloud will be seen in backward-scattered light as a source of a polarized flux that is at least a factor of $\sim 10^6$ fainter than the star or a factor of 10^2-10^3 fainter than what is actually observed (Fig. 3, Table 1). Consequently, the light echo hypothesis is inconsistent with the observed envelope brightness.

Variable Shadowing Hypothesis

Periodic changes in the morphology of the circumstellar envelope may stem from the fact that the outer parts of the envelope are partially obscured from the star by the inner parts of the same envelope. The pattern of obscuration in different directions can change as the radius of the star changes during its pulsations; as a result, different parts of the envelope will change their brightness differently. This explanation was proposed by Kervella et al. (2014) for the semiregular variable star L₂ Pup to explain the observed correlation between the photocenter motion and brightness variations.

If this hypothesis is applicable to V CVn, then there must be a structure in the inner envelope that casts a shadow on the NNE arc at the star's maximum brightness. Assuming that the star reaches its maximum size near the brightness minimum, one might expect that the hypothetical shadowing of the NNE arc would decrease and the latter would become brighter.

However, the color (temperature) of the star also changes during its pulsations. Therefore, the tracks of the NNE and SSE/SSW arcs on the color–flux diagrams should differ within the framework of this

explanation: the NNE arc should become redder as it brightens (the star is at its minimum), while the SSE/SSW arcs, on the contrary, should become bluer when they brighten (the star is at its maximum).

Meanwhile, it follows from Fig. 4 that the color behavior of all envelope components is very similar to and virtually coincides with the color behavior of the star: the brightening is characterized by bluer colors. Thus, we also reject this hypothesis.

Nonradial Pulsation Hypothesis

The pattern of variability of the NNE arc can be naturally explained if we assume that the stellar pulsations from its viewpoint are shifted by half the period compared to the pulsations from the observer's viewpoint. At the same time, from the viewpoint of the SSE/SSW arcs the pulsations appear the same as for the observer. The corresponding model is illustrated in Fig. 5 and suggests a significant deviation of the stellar pulsations from the purely radial ones or, more precisely, the presence of a significant dipolar component.

In this model at maximum brightness the part of the star facing the observer and the SSE/SSW arcs is in a bright state. At the same time, the opposite side of the star facing the NNE arc is dimmed. After half the pulsation period the situation changes to the opposite one. The star now appears faint for the observer and bright for the NNE arc. As a consequence, the latter reaches its maximum brightness. In this case, the contribution of the polarized radiation to the total flux from the object increases. An inverse correlation between flux and polarization is formed.

Previously, Patel et al. (2008) invoked nonradial pulsations as one of the possible qualitative explanations for the unusual polarization variability of the star V1497 Aql. This semiregular variable star occasionally exhibits irregular polarization variations up to 5% at relatively small brightness variations $\approx 0.2^m$. However, no reliable evidence for the existence of dipolar

modes with an amplitude $\Delta V \approx 1.5^m$ has been found in semiregular variable stars. Such pulsations are not predicted theoretically either (see Mosser et al. (2013) and references therein). Therefore, we do not insist on this interpretation.

CONCLUSIONS

We presented the results of our observations of the semiregular variable star V CVn by differential speckle polarimetry at wavelengths of 550, 625, and 880 nm. We found a reflection nebula in polarized light surrounding the star at a characteristic distance of 35 mas, corresponding to 44 AU at the distance of the object. The shape of the nebula deviates significantly from central symmetry: three regions to the north-northeast, south-southeast, and south-southwest of the star are clearly identified in it. The asymmetry of the nebula leads to constancy of the angle of polarization and a relatively high degree of polarization for the object as a whole.

The observations on 20 dates distributed over three pulsation periods show that different regions of the nebula change their brightness with the same period as the star, but with different phase shifts. In particular, the NNE region reaches its maximum brightness when the entire object is at its minimum. At this time the contribution of the scattered and, consequently, polarized radiation to the total flux from the object increases. This leads to the observed inverse correlation between brightness and polarization for V CVn.

Our estimations show that the observed asymmetry of the envelope cannot be produced by the interaction of the stellar wind with the interstellar medium, but is most likely caused by the anisotropy of the mass loss. We provide arguments for the fact that the observed envelope surface brightness variations can be explained neither by Keplerian motion, nor by light echo, nor by variable shadowing. We note that all of the observed features in the behavior of the dust envelope around V CVn could be explained by assuming that the stellar pulsations are considerably nonradial, although we leave the question of whether this explanation is realistic open.

New observations with an angular resolution less than the characteristic size of the object, 35 mas, are required to construct a convincing model for it. Such observations can be performed at a large telescope or on a long-baseline interferometer. For example, speckle interferometry at the 6-m BTA telescope (Maksimov et al. 2009), polarization interferometry at Subaru (Norris et al. 2015), aperture synthesis at CHARA (ten Brummelaar et al. 2009), and LBTI (Skrutskie et al. 2010) can be applied. Both single observations and a monitoring with a periodicity of

≈ 1 month are of value. A spectroscopic monitoring would also allow one to come closer to an understanding of the physical conditions in the atmosphere of this star, for example, to test the hypothesis about its temperature inhomogeneity.

ACKNOWLEDGMENTS

We are grateful to the staff of the Caucasian Observatory of the Sternberg Astronomical Institute for the help with the observed used in this paper and to the referee for the remarks that allowed the quality of the data presentation to be improved. We used observations from the International AAVSO database.

FUNDING

This work was financially supported by RFBR grant nos. 16-32-60065 (B.S. Safonov—the observations and data reduction), 19-02-00611 (A.S. Rastorguev—the interpretation), and the Program for Development of the Moscow State University, Leading scientific School “Physics of Stars, Relativistic Objects, and Galaxies” (A.V. Dodin—the interpretation). The speckle polarimeter of the 2.5-m telescope was created under financial support of the Program for Development of the Moscow State University.

REFERENCES

1. E. de Beck, L. Decin, A. de Koter, K. Justtanont, T. Verhoelst, F. Kemper, and K. M. Menten, *Astron. Astrophys.* **523**, A18 (2010).
2. N. Ben Bekhti, L. Floer, R. Keller, J. Kerp, D. Lenz, B. Winkel, J. Bailin, M. R. Calabretta, et al., *Astron. Astrophys.* **594**, A116 (2016).
3. A. G. A. Brown, A. Vallenari, et al. (Gaia Collab.), *Astron. Astrophys.* **616**, A1 (2018).
4. T. A. ten Brummelaar, H. A. McAlister, S. T. Ridgway, W. G. Bagnuolo, Jr., N. H. Turner, L. Sturmann, J. Sturmann, D. H. Berger, et al., *Astrophys. J.* **628**, 453 (2005).
5. D. van Buren and R. McCray, *Astrophys. J.* **329**, L93 (1988).
6. D. Clarke, *Stellar Polarimetry* (Wiley-VCH, Weinheim, 2010).
7. J. M. Dickey and F. J. Lockman, *Am. Rev. Astron. Astrophys.* **28**, 215 (1990).
8. B. Famaey, D. Pourbaix, A. Frankowski, S. van Eck, M. Mayor, S. Udry, and A. Jorissen, *Astron. Astrophys.* **498**, 627 (2009).
9. S. Kafka, AAVSO Observation Database (2018).
10. P. Kervella, A. Merand, L. Szabados, P. Fouqué, D. Bersier, E. Pompei, and D. Perrin, *Astron. Astrophys.* **480**, 167 (2008).
11. P. Kervella, M. Montargès, S. T. Ridgway, G. Perrin, O. Chesneau, S. Lacour, A. Chiavassa, X. Haubois, and A. Gallenne, *Astron. Astrophys.* **564**, A88 (2014).
12. L. Lindegren, J. Hernandez, A. Bombrun, S. Klioner, U. Bastian, M. Ramos-Lerate, A. de Torres, H. Steidelmüller, et al., *Astron. Astrophys.* **616**, A2 (2018).

13. A. F. Maksimov, Yu. Yu. Balega, V. V. Dyachenko, E. V. Malogolovets, D. A. Rastegaev, and E. L. Semernikov, *Astrophys. Bull.* **64**, 296 (2009).
14. D. C. Martin, M. Seibert, J. D. Neill, D. Schiminovich, K. Forster, R. M. Rich, B. Y. Welsh, B. F. Madore, et al., *Nature (London, U.K.)* **448**, 780 (2007).
15. I. McDonald, A. A. Zijlstra, and M. L. Boyer, *Mon. Not. R. Astron. Soc.* **427**, 343 (2012).
16. R. Montez, Jr., S. Ramstedt, J. H. Kastner, W. Vlemmings, and E. Sanchez, *Astrophys. J.* **841**, 33 (2017).
17. B. Mosser, W. A. Dziembowski, K. Belkacem, M. J. Goupil, E. Michel, R. Samadi, I. Soszyński, M. Vrad, et al., *Astron. Astrophys.* **559**, A137 (2013).
18. H. R. Neilson, R. Ignace, B. J. Smith, G. Henson, and A. M. Adams, *Astron. Astrophys.* **568**, A88 (2014).
19. B. R. M. Norris, P. G. Tuthill, M. J. Ireland, S. Lacour, A. A. Zijlstra, F. Lykou, Th. M. Evans, P. Stewart, and T. R. Bedding, *Nature (London, U.K.)* **484**, 220 (2012).
20. B. Norris, G. Schworer, P. Tuthill, N. Jovanovic, O. Guyon, P. Stewart, and F. Martinache, *Mon. Not. R. Astron. Soc.* **447**, 2894 (2015).
21. F. M. Olnon, E. Raimond, G. Neugebauer, R. J. van Duinen, H. J. Habing, H. H. Aumann, D. A. Beintema, N. Boggess, et al., *Astron. Astrophys. Suppl. Ser.* **65**, 607 (1986).
22. M. Patel, R. D. Oudmaijer, J. S. Vink, J. E. Bjorkman, B. Davies, M. A. T. Groenewegen, A. S. Mirosh-nichenko, and J. C. Motttram, *Mon. Not. R. Astron. Soc.* **385**, 967 (2008).
23. S. D. Price, B. J. Smith, T. A. Kuchar, D. R. Mizuno, and K. E. Kraemer, *Astrophys. J. Suppl. Ser.* **190**, 203 (2010).
24. A. S. Rastorguev, N. D. Utkin, M. V. Zabolotskikh, A. K. Dambis, A. T. Bajkova, and V. V. Bobylev, *Astrophys. Bull.* **72**, 122 (2017).
25. B. S. Safonov, P. A. Lysenko, and A. V. Dodin, *Astron. Lett.* **43**, 344 (2017).
26. B. Safonov, P. Lysenko, M. Goliguzova, and D. Cheryasov, *Mon. Not. R. Astron. Soc.* **484**, 5129 (2019).
27. N. N. Samus, E. V. Kazarovets, O. V. Durlevich, N. N. Kireeva, and E. N. Pastukhova, *Astron. Rep.* **61**, 80 (2017).
28. K. Serkowski and S. J. Shawl, *Astron. J.* **122**, 2017 (2001).
29. K. Sharma, P. Prugniel, and H. P. Singh, *Astron. Astrophys.* **585**, A64 (2016).
30. J. P. Simpson, *Astrophys. J.* **368**, 570 (1991).
31. M. F. Skrutskie, T. Jones, P. Hinz, P. Garnavich, J. Wilson, M. Nelson, E. Solheid, O. Durney, et al., *Proc. SPIE* **7735**, 77353H (2010).
32. P. G. Tuthill, C. A. Haniff, and J. E. Baldwin, *Mon. Not. R. Astron. Soc.* **306**, 353 (1999).

Translated by V. Astakhov